Image-Based Pupil Plane Characterization via Principal Component Analysis for EUVL Tools

Zac Levinson[a], Andrew Burbine[a], Erik Verduijn[b], Obert Wood[b], Pawitter Mangat[b], Kenneth A. Goldberg[c], Markus P. Benk[c], Antoine Wojdyla[c], Bruce W. Smith[a]

[a]Rochester Institute of Technology, 168 Lomb Memorial Drive, Rochester, NY 14623
[b]GLOBALFOUNDRIES, 400 Stone Break Rd. Extension, Malta, NY, 12020
[c]Lawrence Berkeley National Laboratory, One Cyclotron Road, Berkeley, CA 94720

ABSTRACT

We present an approach to image-based pupil plane amplitude and phase characterization using models built with principal component analysis (PCA). PCA is a statistical technique to identify the directions of highest variation (principal components) in a high-dimensional dataset. A polynomial model is constructed between the principal components of through-focus intensity for the chosen binary mask targets and pupil amplitude or phase variation. This method separates model building and pupil characterization into two distinct steps, thus enabling rapid pupil characterization following data collection. The pupil plane variation of a zone-plate lens from the Semiconductor High-NA Actinic Reticle Rreview Project (SHARP) at Lawrence Berkeley National Laboratory will be examined using this method. Results will be compared to pupil plane characterization using a previously proposed methodology where inverse solutions are obtained through an iterative process involving least-squares regression.

Keywords: EUV lithography, EUV aberrations, aberration metrology, image-based aberration metrology, pupil characterization, principal component analysis

INTRODUCTION

Pupil plane characterization and manipulation have played a critical role in image-process optimization at past technology nodes.[1–3] The criticality of pupil characterization continues into EUV lithography (EUVL) with an additional importance placed on understanding the ways that the pupil variation evolves during system operation.[4,5] Interferometric techniques are the de-facto standard of wavefront analysis. These techniques have been demonstrated with sub-nanometer resolution but require the use of additional optics, and are therefore difficult to implement during system use.[6–8] In addition, we have previously shown that amplitude pupil variation in EUV imaging systems can be non-uniform.[9–12]

In the past we have presented an iterative technique to extract the phase and amplitude pupil variation of an EUVL system from images formed by that system.[9,11,13,14] We have demonstrated this technique on several EUV optical systems including the ASML ADT, the ASML NXE:3100 at IMEC, and most recently the Semiconductor High-NA Actinic Reticle Review Project (SHARP), an EUV mask microscope at Lawrence Berkeley National Laboratory.[11,12,14] While the image-based technique is designed to minimize scanner and metrology tool usage, the iterative algorithm can require hours of computation to obtain both the amplitude and phase pupil variation.[11,14]

Using a new algorithm based on principal component analysis (PCA) we are able to separate the model building and wavefront analysis steps. Although this results in a potentially lengthy model building step, the wavefront analysis step can be completed in under half a second. Model building only needs to be completed once for each imaging system. In this paper we aim to show that this technique is comparable to the already established iterative method. We will examine the fundamental concepts of this algorithm and present results of a preliminary experiment using the SHARP EUV mask microscope.[15,16]

Extreme Ultraviolet (EUV) Lithography VII, edited by Eric M. Panning, Proc. of SPIE Vol. 9776, 977618 · © 2015 SPIE · CCC code: 0277-786X/15/$18 · doi: 10.1117/12.2219745

THEORY

The transfer of light through an optical system can be represented by its pupil function[17,18],

$$P(u,v) = \alpha(u,v)e^{i2\pi W(u,v)} \tag{1}$$

Where (u,v) represent normalized Cartesian frequency coordinates, $\alpha(u,v)$ represents the pupil amplitude function, and $W(u,v)$ represents the pupil phase function. It is customary to expand the phase function in a Fourier-Zernike series as[18,19],

$$W(u,v) = \sum_{n=0}^{\infty} a_n Z_n(\rho,\phi) \tag{2}$$

Where (ρ,ϕ) represents polar coordinates defined in terms of (u,v), and Z_n represents the nth Zernike polynomial.[19,20] In traditional aberration theory the pupil amplitude function is assumed to be given by a uniformly transmitting top-hat profile. We have shown that this is inadequate to describe the pupil amplitude function in EUVL systems. Therefore, we redefine the amplitude function in terms of a separate Fourier-Zernike series given as,

$$\alpha(u,v) = 1 + \sum_{n=0}^{\infty} b_n Z_n(\rho,\phi) \tag{3}$$

We have identified a number of pattern types, already present on most masks, which are sensitive to specific types of Zernike polynomials, as shown in Figure 1a. If a certain aberration is present, then there will be a phase or amplitude difference between the measurement sites of these targets.[14] The pupil variation of an optical system can then be extracted via the images of these targets as in the algorithm described by Figure 1b.

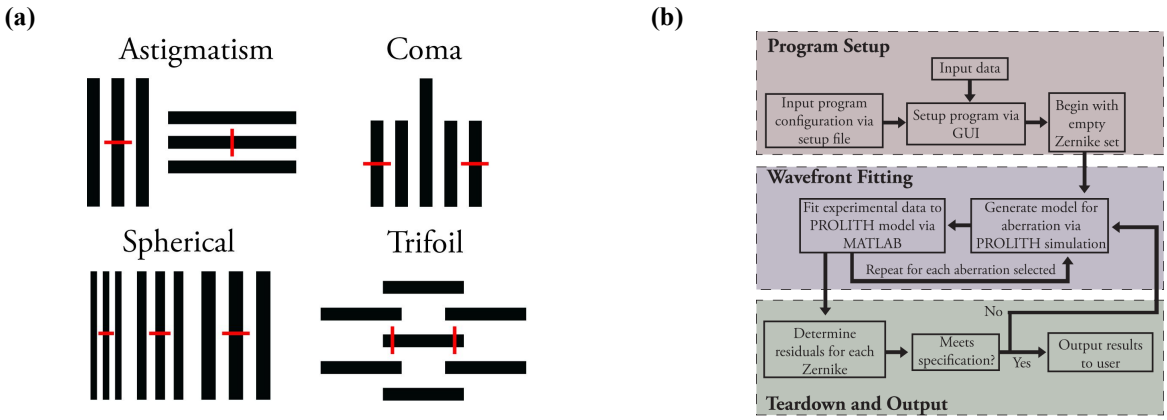

Figure 1. (a) Examples of metrology targets for each primary aberration. The red lines denote measurement locations. The aberration is interrogated by the CD difference at measurement sites. (b) A flowchart for the iterative algorithm of image-based pupil characterization.

To begin, we assume that the system is aberration free. A number of aerial image simulations are computed and a model is fit to these simulations via non-linear least squares. This model can then be inverted to fit to experimental data (either aerial image or CD data) and obtain an initial guess for that particular aberration. This process is repeated for each aberration to obtain an initial guess for the aberrated wavefront. Finally, the process repeats until the algorithm converges on a solution for the pupil variation. This technique is presented in more detail in our earlier report.[14]

Principal component analysis (PCA) is a statistical technique to identify the directions of highest variation in a high dimensional dataset.[21] To begin, we must obtain the dataset and subtract the mean. Next, the covariance matrix is computed and decomposed into eigenvectors and eigenvalues. Finally, the eigenvectors are sorted by decreasing eigenvalue.[22] This process is depicted in Figure 2 where PCA was used to analyze data representing a line in $\mathbf{R}^3$ with Gaussian noise. The direction of highest variation is given by the eigenvector with the highest eigenvalue and is termed PC1. In Figure 2 this is the direction which appears to be a least-squares line of best fit to the data. In actuality, this direction minimizes the error orthogonal to the data—not orthogonal to the axis, as in least-squares regression.

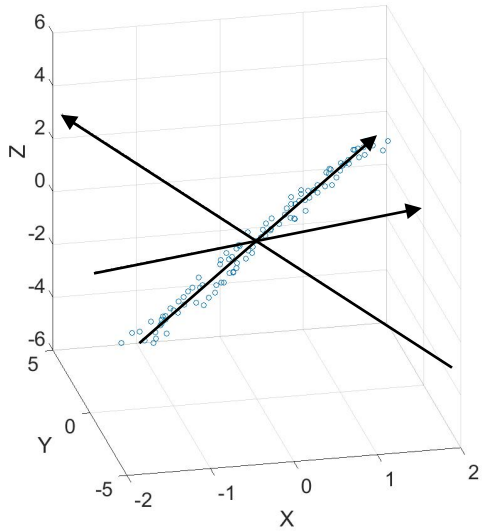

Figure 2. Data representing a line in $\mathbf{R}^3$ with Gaussian noise (blue circles) with the orthogonal directions of highest variation identified (black arrows) via PCA.

To apply this technique to lithography we will consider a 1D aerial image through focus, which we call a through-focus intensity volume, as in Figure 3a. This intensity volume is part of a higher dimensional dataset when aberrations are present in the optical system. For example, a system with an unknown amount of spherical aberration can be described by a four dimensional dataset, as shown in Figure 3b. This dataset can be decomposed using PCA and each principal component can be interpreted as its own intensity volume, as shown in Figure 4. We will refer to these principal components as *eigenvolumes*.

The eigenvolume shows the aerial image variation caused by a certain aberration. This can be seen in Figure 4 where the first eigenvolume shows the maximum intensity of lines increasing with positive defocus. This has the effect of shifting the best focus of that pattern. The eigenvolumes of the primary phase aberrations are given in Figures 5–7. It can be seen from the eigenvolumes that astigmatism causes an orientation dependent change in best focus, spherical aberration causes a pitch dependent change in best focus, coma causes placement error and asymmetric smear across the field, and finally trefoil causes a CD difference in patterns with 60° symmetry. It is also apparent that even-parity phase polynomials (as given in Figures 5 and 6) cause through-focus variation unlike odd-parity phase polynomials (as given in Figure 7).

We can now determine the action of amplitude aberrations using this same type of analysis. The eigenvolumes of the primary Zernike polynomials as applied to amplitude pupil variation (given as $Z_A n$) are given in Figures 8–10. It is seen that, unlike their phase counterparts, the even-parity Zernike amplitude polynomials do not cause through-focus variation, while the odd-parity components do. $Z_A 5$ and $Z_A 6$ can be seen to cause orientation dependent changes in contrast, $Z_A 9$ causes pitch dependent changes in contrast, $Z_A 7$ and $Z_A 8$ cause a field and focus dependent pattern smear, and finally $Z_A 10$ and $Z_A 11$ cause focus dependent changes in contrast and placement error.

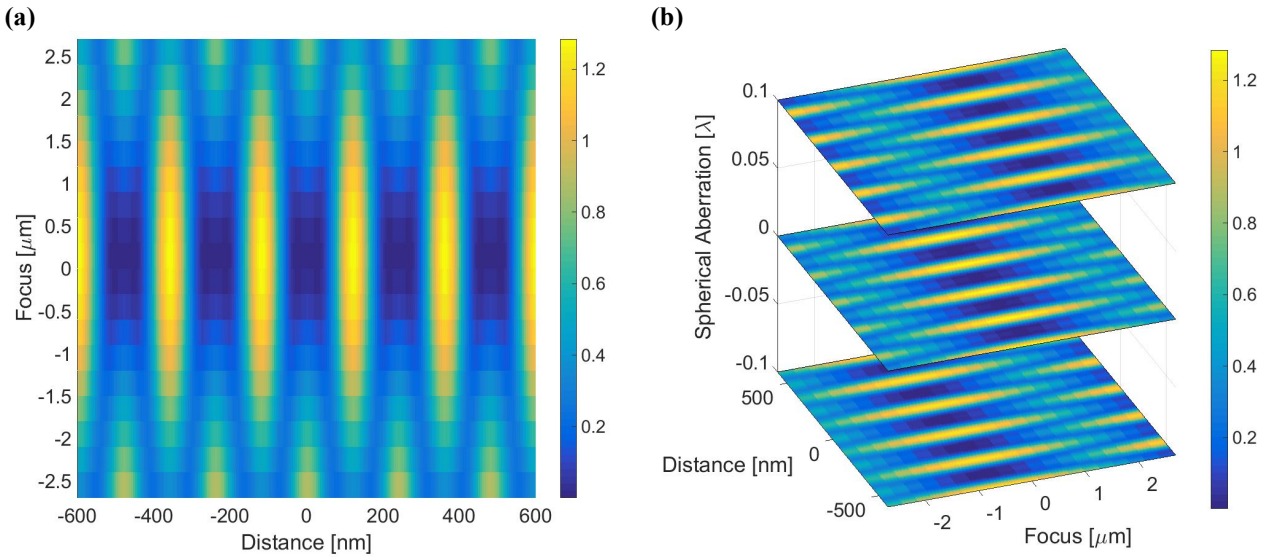

Figure 3. A 1D aerial image through defocus (a) represents an intensity volume which is part of a higher dimensional space (b) when aberrations are present in an optical system.

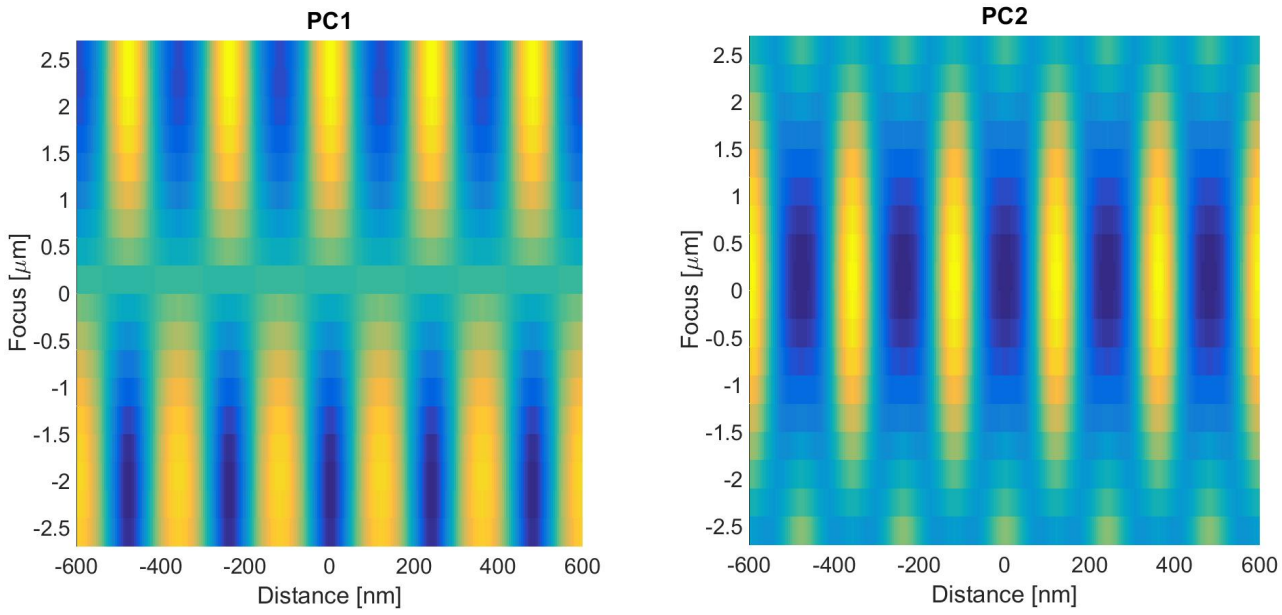

Figure 4. The first two principal components, or eigenvolumes, of the dataset shown in Figure 3.

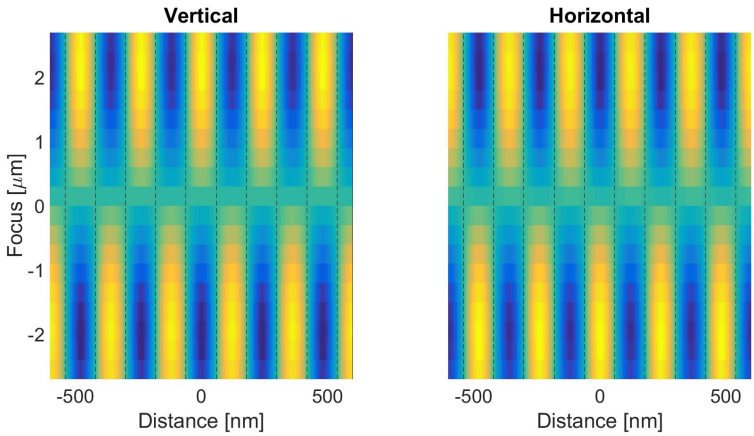

Figure 5. Eigenvolume for a 60 nm pitch line/space array with astigmatism. Because the action of astigmatism is orientation dependent the eigenvolume in this case consists of both plots together. Coordinates are given at the mask level with the dashed lines representing the mask edge.

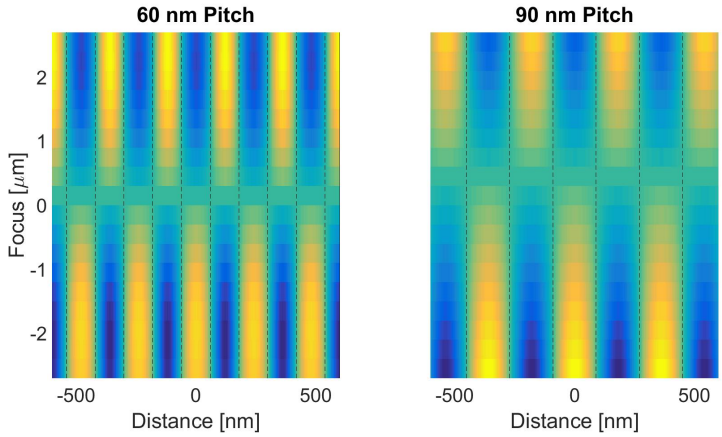

Figure 6. Eigenvolume for a 30 nm line at 60 nm pitch and 90 nm pitch with spherical aberration. Because the action of spherical aberration is pitch dependent the eigenvolume in this case consists of both plots together. Coordinates are given at the mask level with the dashed lines representing the mask edge.

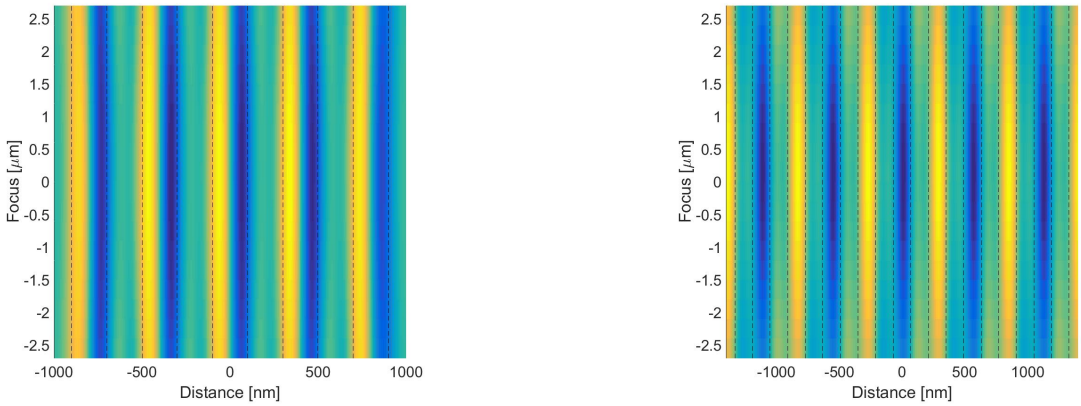

Figure 7. Eigenvolume for a 50 nm CD five-bar pattern with coma (left) and eigenvolume for a 35 nm brick wall structure with trefoil (right). The left most feature in this trefoil eigenvolume represents the right side of a bar. Coordinates are given at the mask level with the dashed lines representing the mask edge.

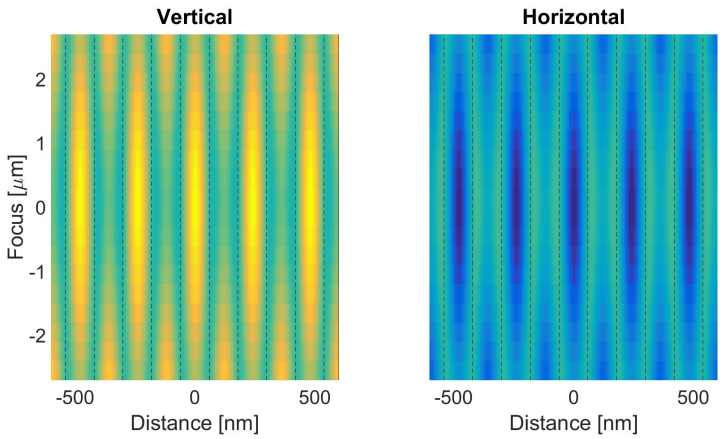

Figure 8. Eigenvolume for a 60 nm pitch line/space array with Z_A5 and Z_A6. Because the action of these aberrations are orientation dependent the eigenvolume in this case consists of both plots together. Coordinates are given at the mask level with the dashed lines representing the mask edge.

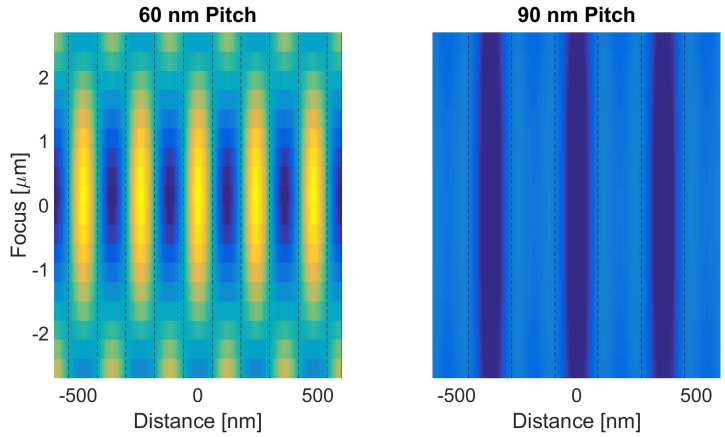

Figure 9. Eigenvolume for a 30 nm line at 60 nm pitch and 90 nm pitch with Z_A9. Because the action of Z_A9 is pitch dependent the eigenvolume in this case consists of both plots together. Coordinates are given at the mask level with the dashed lines representing the mask edge.

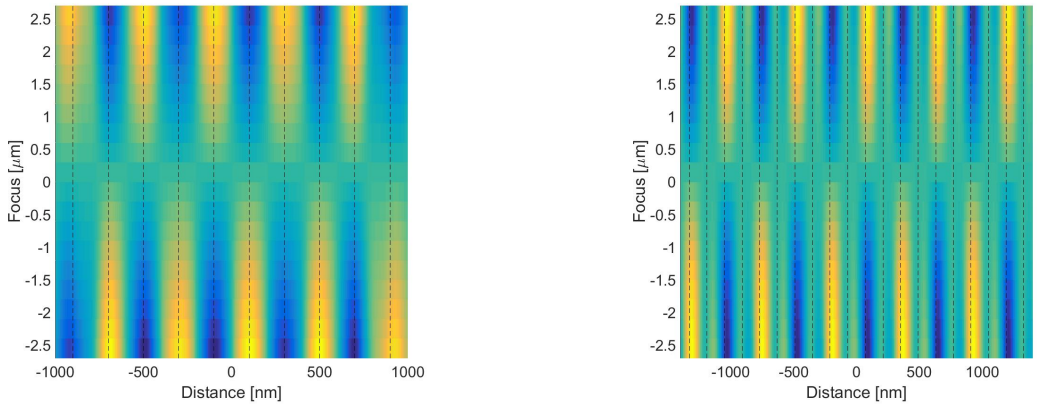

Figure 10. Eigenvolume for a 50 nm CD five-bar pattern with Z_A7 and Z_A8 (left) and the eigenvolume for a 35 nm brick wall structure with Z_A10 and Z_A11 (right). The left most feature of the Z_A10 and Z_A11 eigenvolume represents the right side of a bar. Coordinates are given at the mask level with the dashed lines representing the mask edge.

All of this can be applied to inverse pupil solutions as follows: 1) a set of intensity volumes is simulated corresponding to a full factorial experiment, 2) this dataset is analyzed using PCA, 3) each simulated intensity volume is projected onto the eigenvolumes obtained via PCA, 4) a model is constructed between the treatment combinations and projection coefficients. This process is detailed graphically in Figure 11.

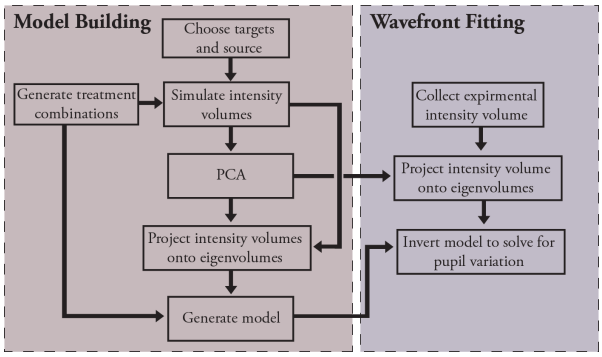

Figure 11. A flowchart for the PCA-based algorithm of image-based pupil characterization.

More specifically, each model consists of a system of polynomial equations fit to the projection coefficients via non-linear least squares. Assuming that the relationship between treatment combinations and projection coefficients is linear, this model can be formalized as,

$$C^{(n)} = \mathbf{tc} \cdot \beta^{(\mathbf{n})} + \bar{C}^{(n)} \tag{4}$$

Where $C^{(n)}$ is the projection of each intensity volume onto the n^{th} eigenvolume, $\beta^{(n)}$ represents the model coefficients, and $\bar{C}^{(n)}$ represents the mean projection coefficient onto the n^{th} eigenvolume. In the linear case this could be formed into a matrix equation as,

$$C^{(n)} = \begin{bmatrix} tc_{11} & tc_{12} & tc_{13} & \dots & tc_{1n} \\ tc_{21} & tc_{22} & tc_{23} & \dots & tc_{2n} \\ \vdots & \vdots & \vdots & \ddots & \vdots \\ tc_{m1} & tc_{m2} & tc_{m3} & \dots & tc_{mn} \end{bmatrix} \cdot \begin{bmatrix} \beta_1^{(n)} \\ \beta_2^{(n)} \\ \vdots \\ \beta^{(n)} \end{bmatrix} + \bar{C}^{(n)} \tag{5}$$

Finally, an experimental intensity volume can be projected onto the simulated eigenvolumes and the model can be inverted as,

$$\mathbf{X} = \beta^{-\mathbf{1}}(\hat{\mathbf{C}} - \bar{C}) \tag{6}$$

Where $\hat{C}$ is the projection of an experimental intensity volume onto the model eigenvolumes. Some researchers have presented similar models where only those principal components which vary linearly are chosen for the model.[23,24] Choosing only linear principal components limits the accuracy of this approach though. In reality the relationship between treatment combinations and projection coefficients is often non-linear. The same techniques can be applied but instead a higher order polynomial must be used. In the non-linear case the model must be inverted by solving the system of equations numerically. In our four-dimensional example with spherical aberration the forward model is generalized as,

$$C^{(1)} = \bar{C}^{(1)} + \beta_1^{(1)} a_9 + \beta_2^{(1)} a_9^2 + \dots \tag{7}$$

EXPERIMENTAL APPROACH

The Semiconductor High-NA Actinic Reticle Review Project (SHARP) is an EUV mask microscope at Lawrence Berkeley National Laboratory. A schematic view of the system is shown in Figure 12. SHARP forms a magnified image of an EUVL mask at 13.5 nm wavelength onto a CCD sensor using a Fresnel zone plate lens. The lens is interchangeable and a number of numerical apertures are available from 0.25-0.625 4xNA. Additionally, a wide range of illumination conditions are available through the use of a MEMs mirror (M_A in Figure 12).

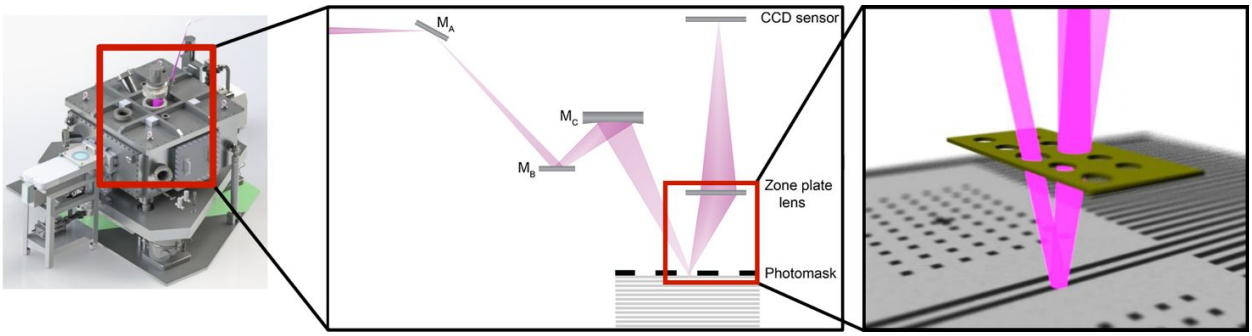

Figure 12. A schematic view of the SHARP microscope at the Advanced Light Source. EUV light at 13.5 nm from a bending magnet is focused on the photomask. The photomask is imaged on a CCD sensor using Fresnel zone plate lens.

The target CDs of the structures used for this experiment are given Table 1. These values were determined by calculating the pitch required to sample the desired pupil location. Structures were chosen to sample the ρ=0.5 and ρ=0.9 pupil zones. All data was collected using a 0.25 4xNA lens using a 0.1σ conventional illuminator. This source was chosen to resemble a coherent source, yet introduces a small amount of pupil averaging. Each target was imaged through its full depth of focus with the smallest step size available—±2.7 μm in 0.3 μm steps.

Table 1. CDs of the metrology targets used for pupil function extraction on SHARP.

Aberration Name	Structure Type	Target CD [nm]
Astigmatism 90° (Z5)	Vertical/Horizontal Lines	30
Astigmatism 45° (Z6)	45°/135° Lines	30
Coma X (Z7)	Vertical 5-bar	50
Coma Y (Z8)	Horizontal 5-bar	50
Spherical (Z9)	Line through pitch	30
Trefoil X (Z10)	Horizontal T-Bar	35
Trefoil Y (Z11)	Vertical T-Bar	35

Images were analyzed using custom image processing software written in MATLAB.[25] The images are registered to eliminate stage errors and the region of interest was interpolated using Fourier interpolation. Images were collected at approximately 15 nm/px and interpolated to approximately 5 nm/px. The aerial image is approximated by finding the column-wise median of the interpolated region, then normalized such that the intensity volume peaks at the ideal value at best focus—1.29 for three-beam imaging.

Models were created for the PCA-based pupil variation retrieval algorithm using vector aerial image simulations (PROLITH[26]). A 10^2 full factorial experiment was run for each Zernike polynomial using a phase design unit of 100 mλ and an amplitude design unit of 50%. The best polynomial model was chosen using Akaike information criterion (AIC), an information theoretic approach to quantifying over-fitting risk.[27] Finally, pupil amplitude and phase variation were extracted using both the PCA-based and iterative algorithms.

RESULTS AND ANALYSIS

The required polynomial order (along with its associated AIC weight) and the model RMSE are given in Table 2. The RMSE for both phase and amplitude are on the order of 0.2 mλ and percent, respectively. This is comparable to past studies using the iterative algorithm. Models were built on a machine using a 3.6 GHz quad-core Intel i7 processor and 16 GB of RAM and the total runtime to build all models was 20 hours.

Table 2. Required polynomial orders, and their associated RMSE for phase and amplitude variation, for each Zernike polynomial.

Name	Polynomial Order	Phase RMSE [mλ]	Amplitude RMSE [%]
Z_5	6 (0.632 AIC weight)	0.18	0.35
Z_6	5 (0.500 AIC weight)	0.19	0.25
Z_7/Z_8	4 (0.496 AIC weight)	0.10	0.20
Z_9	6 (0.995 AIC weight)	0.10	0.15
Z_{10}/Z_{11}	N/A	N/A	N/A

Accurate models could not be built for Z_{10} and Z_{11} due to very small eigenvalues using the targets picked out for the iterative algorithm. In PCA the eigenvalues of each eigenvector correspond to the strength of a certain direction of variation. Therefore, a small eigenvalue makes it difficult to identify this type of variation in the inverse direction using this algorithm. The iterative algorithm has the advantage of using a predictor-corrector approach, enabling it to still accurately extract Z_{10} and Z_{11}.

A comparison of the pupil variation extracted with both the iterative and PCA-based algorithms is given in Table 3. The iterative algorithm took 3.2 hours to converge on a solution on the same machine described above, while the PCA-based algorithm took 0.2 seconds to obtain an inverse solution. The results obtained using both methods are very similar with the exception of Z_8 in phase (coma Y).

Table 3. A comparison of the extracted phase and amplitude variation using both the iterative algorithm and PCA-based algorithm.

Name	Iterative Phase [mλ]	Iterative Amplitude [%]	PCA Phase [mλ]	PCA Amplitude [%]
Z_5	-1.0	+14.9	-3.5	+5.1
Z_6	-3.5	+0.3	-2.4	+0.4
Z_7	0.0	-10.0	-0.8	-20.1
Z_8	0.0	-15.4	+28.3	+4.3
Z_9	+2.7	+2.8	+1.8	+4.9
Z_{10}	0.0	-10.3	N/A	N/A
Z_{11}	-23.2	+3.9	N/A	N/A

This apparent discrepancy may be attributable to the lack of Z_{11} (trefoil Y) in the PCA-based models. Patterns sensitive to coma will also be sensitive to trefoil. It is therefore likely that the extracted +28.3 mλ of coma Y can actually be attributed to the -23.2 mλ of trefoil Y which were extracted using the iterative procedure. The sign between the two results also lends credence to this explanation.

CONCLUSIONS

We are developing an algorithm for rapid pupil characterization enabled via principal component analysis (PCA). This algorithm was compared to a previously demonstrated iterative algorithm. Both techniques extract the pupil amplitude and phase variation of an EUVL system from images formed by that system. We have demonstrated the new PCA-based algorithm experimentally using data from the SHARP EUV mask microscope. While the iterative algorithm took 3.2 hours to find a solution, the PCA-based algorithm obtained its solution in 0.2 seconds. A 20-hour model building step is necessary to use the PCA-based algorithm but this only need to be completed once. Results between the two algorithms match closely with the exception of coma Y. This is likely due to this pattern being sensitive to both coma Y and trefoil Y, combined with the omission of trefoil from the models due to small eigenvalues. It should be noted that this is not a theoretical problem with the technique, but rather a practical problem which can be solved with further modeling. In the future we hope to expand this PCA-based algorithm to CD data to enable rapid full-pupil characterization through resist images.

ACKNOWLEDGEMENTS

The authors would like to thank KLA Tencor for use of the PROLITH™ lithography simulator.

REFERENCES

[1] Kempsell Sears, M., Fenger, G., Mailfert, J.., Smith, B., "Extending SMO into the lens pupil domain," Proc. SPIE 7973, 79731B – 79731B – 9 (2011).

[2] Kempsell Sears, M., Bekaert, J.., Smith, B. W., "Pupil wavefront manipulation for optical nanolithography," Proc. SPIE 8326, 832611–832611 – 11 (2012).

[3] Baylav, B., Maloney, C., Levinson, Z., Bekaert, J., Vaglio Pret, A.., Smith, B. W., "Impact of pupil plane filtering on mask roughness transfer," J. Vac. Sci. Technol. B Microelectron. Nanometer Struct. **31**(6), 06F801 (2013).

[4] Bakshi, V., [EUV Lithography], SPIE, 1000 20th Street, Bellingham, WA 98227-0010 USA (2008).

[5] Krautschik, C. G., Ito, M., Nishiyama, I.., Mori, T., "Quantifying EUV imaging tolerances for the 70-, 50-, 35-nm modes through rigorous aerial image simulations," Proc. SPIE 4343, 524–534 (2001).

[6] Foucault, L., "Description des procedees employes pour reconnaitre la configuration des surfaces optiques," C R Acad Sci 47, 958ff (1858).

[7] Linnik, W. P., "A simple interferometer for the investigation of optical systems," Proc Acad. Sci USSR **1**, 208 (1933).

[8] Naulleau, P. P., Goldberg, K. A.., Bokor, J., "Extreme ultraviolet carrier-frequency shearing interferometry of a lithographic four-mirror optical system," J. Vac. Sci. Technol. B **18**(6), 2939–2943 (2000).

[9] Zavyalova, L. V., Smith, B. W., Suganaga, T., Matsuura, S., Itani, T.., Cashmore, J. S., "In-situ aberration monitoring using phase wheel targets," Proc. SPIE 5377, 172 (2004).

[10] Fenger, G. L., Raghunathan, S., Sun, L., Wood, O. R.., Smith, B. W., "EUVL resist-based aberration metrology," Proc. SPIE 8679, 86790P – 86790P – 10, (2013).

[11] Levinson, Z., Raghunathan, S., Verduijn, E., Wood, O., Mangat, P., Goldberg, K., Benk, M., Wojdyla, A., Philipsen, V., et al., "A method of image-based aberration metrology for EUVL tools," Proc. SPIE 9422, 942215–942215 (2015).

[12] Levinson, Z., Verduijn, E., Wood, O. R., Mangat, P., Goldberg, K. A., Benk, B. Markus P., Wojdyla, A.., Smith, B. W., "Measurement of EUVL Pupil Amplitude and Phase Variation via Image-Based Methodology," *In Preparation* (2016).

[13] Smith, B. W., "Method for aberration detection and measurement," *US Patent* **US7136143 B2** (2006).

[14] Fenger, G. L., Sun, L., Raghunathan, S., Wood, O. R.., Smith, B. W., "Extreme ultraviolet lithography resist-based aberration metrology," J. MicroNanolithography MEMS MOEMS **12**(4), 043001–043001 (2013).

[15] Goldberg, K. A., Mochi, I., Benk, M., Allezy, A. P., Dickinson, M. R., Cork, C. W., Zehm, D., Macdougall, J. B., Anderson, E., et al., "Commissioning an EUV mask microscope for lithography generations reaching 8 nm," Proc. SPIE 8679, 867919–867919 – 10 (2013).
[16] Goldberg, K. A., Benk, M. P., Wojdyla, A., Mochi, I., Rekawa, S. B., Allezy, A. P., Dickinson, M. R., Cork, C. W., Chao, W., et al., "Actinic mask imaging: recent results and future directions from the SHARP EUV microscope," Proc. SPIE 9048, 90480Y – 90480Y – 10 (2014).
[17] Smith, B. W., "Optics for Photolithography," [Microlithography: Science and Technology], B. W. Smith and K. Suzuki, Eds., CRC Press (2007).
[18] Born, M.., Wolf, E., [Principles of Optics], 7th ed., Press Syndicate of the University of Cambridge (1999).
[19] Nijboer, B., "The Diffraction Theory of Aberrations" (1942).
[20] von Zernike, F., "Beugungstheorie des schneidenver-fahrens und seiner verbesserten form, der phasenkontrastmethode," Publica 1, 689–704 (1934).
[21] Pearson F.R.S, K., "On lines and planes of closest fit to systems of points in space," Philos. Mag. Ser. 6 **2**(11), 559–572 (1901).
[22] Smith, Lindsay I., "A tutorial on Principal Components Analysis" (2002).
[23] Duan, L., Wang, X., Yan, G.., Bourov, A., "Practical application of aerial image by principal component analysis to measure wavefront aberration of lithographic lens," J. MicroNanolithography MEMS MOEMS **11**(2), 023009–1 (2012).
[24] Xu, D., Wang, X., Bu, Y., Duan, L., Yan, G., Yang, J.., Burov, A. Y., "In situ aberration measurement technique based on multi-illumination settings and principal component analysis of aerial images," Chin. Opt. Lett. **10**(12), 121202–121202 (2012).
[25] Levinson, Z., Burbine, Andrew., Verduijn, E., Wood, O., Mangat, P., Goldberg, K., Benk, M., Wojdyla, A.., Smith, Bruce W., "Image-based pupil plane characterization via principal component analysis for EUVL tools," Proc. SPIE 9776, **977645** (2016).
[26] KLA Tencor., "PROLITH," Version X5.1, <http://www.kla-tencor.com/lithography-modeling/chip-prolith.html> (2015).
[27] Burbine, A., Fryer, D.., Sturtevant, J., "Akaike information criterion to select well-fit resist models," Proc. SPIE 9427, 94270J – 94270J – 7 (2015).